





Article

Inverse Magnetocaloric Effect in Heusler $\text{Ni}_{44.4}\text{Mn}_{36.2}\text{Sn}_{14.9}\text{Cu}_{4.5}$ Alloy at Low Temperatures

Alexander P. Kamantsev ^{1,*}, Yuriy S. Koshkid'ko ², Ruslan Yu. Gaifullin ³, Irek I. Musabirov ³, Anatoliy V. Koshelev ⁴, Alexey V. Mashirov ¹, Vladimir V. Sokolovskiy ^{5,6}, Vasiliy D. Buchelnikov ⁵, Jacek Ćwik ² and Vladimir G. Shavrov ¹

- ¹ Kotelnikov Institute of Radioengineering and Electronics of Russian Academy of Sciences, 125009 Moscow, Russia; mashirov@cplire.ru (A.V.M.); shavrov@cplire.ru (V.G.S.)
- ² Institute of Low Temperature and Structure Research of Polish Academy of Sciences, 50-422 Wrocław, Poland; y.koshkidko@intibs.pl (Y.S.K.); j.cwik@intibs.pl (J.Ć.)
- ³ Institute for Metals Superplasticity Problems of Russian Academy of Sciences, 450001 Ufa, Russia; gaifullin_1998@bk.ru (R.Y.G.); irekmusabirov@imsp.ru (I.I.M.)
- ⁴ Institute of Experimental Mineralogy of Russian Academy of Sciences, 142432 Chernogolovka, Russia; anatolkosh@mail.ru
- ⁵ Department of Condensed Matter Physics, Chelyabinsk State University, 454001 Chelyabinsk, Russia; vsokolovsky84@mail.ru (V.V.S.); buche@csu.ru (V.D.B.)
- ⁶ Academic Research Center for Energy Efficiency, National University of Science and Technology "MISIS", 119049 Moscow, Russia
- * Correspondence: kama@cplire.ru

Abstract: Direct measurements of the magnetocaloric effect were performed in a Heusler $\text{Ni}_{44.4}\text{Mn}_{36.2}\text{Sn}_{14.9}\text{Cu}_{4.5}$ alloy at cryogenic temperatures in magnetic fields up to 10 T. The maximum value of the inverse magnetocaloric effect in a 10 T field was $\Delta T_{\text{ad}} = -2.7$ K in the vicinity of the first-order magnetostructural phase transition at $T_0 = 117$ K. Ab initio and Monte Carlo calculations were performed to discuss the effect of Cu doping into a Ni-Mn-Sn compound on the ground-state structural and magnetic properties. It is shown that with increasing Cu content the martensitic transition temperature decreases and the Curie temperature of austenite slightly increases. In general, the calculated transition temperatures and magnetization values correlated well with the experimental ones.

Keywords: metamagnetic phase transition; magnetocaloric effect; Heusler alloys; Monte Carlo calculations



Citation: Kamantsev, A.P.; Koshkid'ko, Y.S.; Gaifullin, R.Y.; Musabirov, I.I.; Koshelev, A.V.; Mashirov, A.V.; Sokolovskiy, V.V.; Buchelnikov, V.D.; Ćwik, J.; Shavrov, V.G. Inverse Magnetocaloric Effect in Heusler $\text{Ni}_{44.4}\text{Mn}_{36.2}\text{Sn}_{14.9}\text{Cu}_{4.5}$ Alloy at Low Temperatures. *Metals* **2023**, *13*, 1985. <https://doi.org/10.3390/met13121985>

Academic Editors: Victorino Franco, Yan Feng, Changlong Tan and Kun Zhang

Received: 6 October 2023
Revised: 28 November 2023
Accepted: 4 December 2023
Published: 7 December 2023



Copyright: © 2023 by the authors. Licensee MDPI, Basel, Switzerland. This article is an open access article distributed under the terms and conditions of the Creative Commons Attribution (CC BY) license (<https://creativecommons.org/licenses/by/4.0/>).

1. Introduction

The hopeful idea of solid-state magnetic cooling (SMC) through the adiabatic demagnetization of paramagnetic Gd salts was used in 1933 to develop novel methods to achieve low temperatures below 1 K [1]. SMC is based on the magnetocaloric effect (MCE), which is a reversible change in the temperature ΔT_{ad} (under adiabatic conditions) or entropy ΔS_{iso} (under isothermal conditions) of a magnetic material due to external magnetic field changes [2,3]. The MCE is an efficient apparatus for the investigation of magnetic phase transitions (PTs), which are among the most exigent problems in modern solid-state physics. The maximum MCE is reached in the vicinity of magnetic PTs [3,4]. Magnetic materials with magnetic PTs in the required working temperature range are chosen for SMC. The promising applications of SMC at low temperatures, particularly for the liquefaction of gases such as N_2 , He, H_2 or natural gases, have been mentioned in [5–8]. The advantage of such materials for SMC at low temperatures is connected with the increase in their magnetic heat capacity in the magnetic PT region. It becomes comparable to (and sometimes exceeds) the crystal lattice heat capacity. This fact makes SMC more promising at low temperatures, where the lattice heat capacity of metals is much higher than that at room temperature. It is currently accepted that low (cryogenic) temperatures are those below 120 K [9].

The MCE can be either direct or inverse under the magnetization of a magnetic material [2–4]. The direct MCE is an increase in temperature at adiabatic conditions or a decrease in entropy at isothermal conditions. Conversely, the inverse MCE is a positive isothermal change in entropy or a negative adiabatic change in temperature under magnetization. Both the direct and inverse MCE can be applied for SMC at low temperatures. The inverse MCE can be applicable when it is necessary to quickly cool a magnetic field area. For this purpose, a magnetic field is simply applied to the working body. Thus, the working body will cool down, and it will also cool the magnetic field area. This effect can be applied to the cooling of a superconducting magnet and the surrounding liquefied gas, making it possible to reduce the expenditure of liquefied gas.

The rare-earth metals [4] and their intermetallic compounds [10] are the most promising materials for SMC at low temperatures. The magnetostructural PTs in such alloys are commonly observed at temperatures above 120 K [2]. Most often, they show a direct MCE in the vicinity of the PTs. The inverse MCE is observed in their intermetallic compounds with antiferromagnetic (AFM) ordering: RCu_2 , R_2Fe_{17} , RFe_3 (R—heavy rare-earth metal) [10–12], Gd-based alloys (Gd_2In [13], GdRuSi [14]). The inverse MCE can also be observed as a result of magnetization rotation upon the magnetization of a highly anisotropic single-crystal sample along the hard magnetization axis in, for example, RCo_5 [15] and $\text{Tb}_2\text{CoMnO}_6$ [16]. However, the rare-earth metals are expensive, and their compounds are breakable and rapidly oxidize in air, so they are difficult to use in the proposed SMC scheme.

Significant inverse MCE can be observed in several ferromagnetic (FM) Heusler alloys based on Ni–Mn–Z (Z = In, Sn, Sb), but they usually show the effect closer to room temperature [17–22]. Some Heusler alloy compositions show the inverse MCE at low temperatures, for example, the Ni(-Co)-Mn-Ti Heusler alloys [23]. In general, the Heusler alloys are cheap to produce, as they consist of inexpensive chemical elements and do not require long-term heat treatment, unlike alloys based on expensive rare-earth elements. Therefore, the goal of our work was to study the inverse MCE at low temperatures in a Heusler composition, which was chosen according to [24]. We investigated a $\text{Ni}_{44.4}\text{Mn}_{36.2}\text{Sn}_{14.9}\text{Cu}_{4.5}$ Heusler alloy with the inverse MCE at low temperature for SMC and try to explain its properties theoretically in this paper.

2. Materials and Methods

2.1. Samples Characterization

A polycrystalline ingot of the $\text{Ni}_{44.4}\text{Mn}_{36.2}\text{Sn}_{14.9}\text{Cu}_{4.5}$ Heusler alloy was synthesized via the argon arc-melting method from high-purity elements. The ingot was remelted seven times to eliminate the chemical segregation of the composition. The obtained ingot had a mass of about 80 g. The samples, in the form of 1 mm thick plates, were placed in quartz ampoules, in which a vacuum of about 10 Pa was created. The ampoules were then sealed. Previous research found that the melting point of this alloy is 1313 K [25]; therefore, the temperature of the homogenization annealing was selected as 1133 K. The sealed samples were subjected to homogenization annealing for 24 h, and then they were quenched in water.

The quenched plates were prepared for structure analysis by electropolishing in an electrolyte with 90% n-butyl alcohol ($\text{C}_4\text{H}_9\text{OH}$) and 10% HCl. X-ray diffraction and X-ray phase analyses were performed on a “Rigaku” Ultima V X-ray diffractometer using $\text{Cu-K}\alpha$ radiation. The crystal structure of the studied sample at room temperature was cubic (space group $Fm-3m$), with lattice parameter $a_0 = 5.991 \text{ \AA}$. The analyses of the microstructure and elemental composition were carried out on a “Tescan” Vega 3-SBH scanning electron microscope (SEM) equipped with sensors for backscattered electrons and energy-dispersive X-ray (EDX) analysis on a “Oxford Instruments” X-Act. The specimens were prepared by electropolishing in an electrolyte with 90% n-butyl alcohol ($\text{C}_4\text{H}_9\text{OH}$) and 10% HCl. The microstructure of the alloy as observed via SEM is represented by a single-phase state in Figure 1a. The dark points on the thin section are etching pits. The grains have a size on the order of 100 μm , according to the orientational contrast. The microstructure can generally

be characterized as equiaxed. The unblurred contrast means that the grain boundaries are high-angle. The chemical element maps of the section area obtained by EDX analysis are presented in Figure 1b. The distribution of the Ni, Mn, Sn and Cu is uniform, and there are no areas with the localization of any elements. It can be concluded that annealing at 1133 K for 24 h followed by quenching made it possible to obtain a single-phase-state sample, although this determination is constrained by the limitations of EDX analysis.

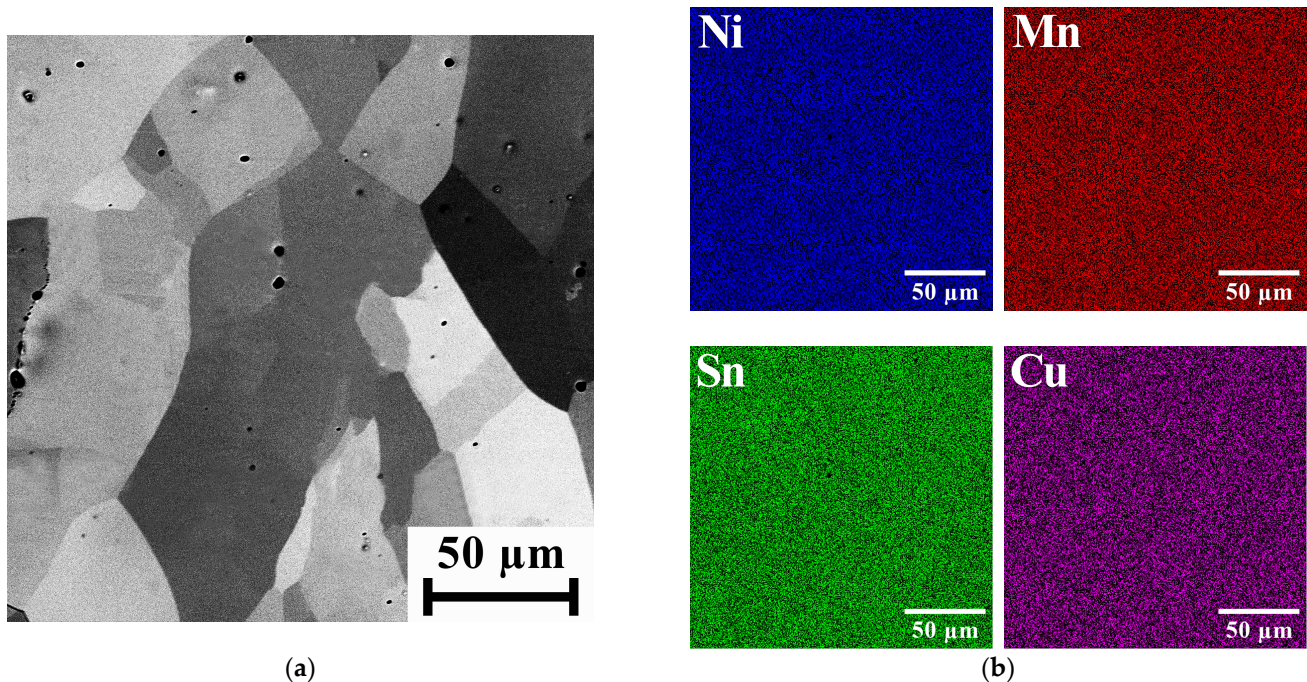


Figure 1. (a) Microstructure of the $\text{Ni}_{44.4}\text{Mn}_{36.2}\text{Sn}_{14.9}\text{Cu}_{4.5}$ Heusler alloy, obtained via SEM. (b) Maps of the chemical element distribution of the section area of the $\text{Ni}_{44.4}\text{Mn}_{36.2}\text{Sn}_{14.9}\text{Cu}_{4.5}$ Heusler alloy, obtained via EDX analysis.

The magnetic properties of the $\text{Ni}_{44.4}\text{Mn}_{36.2}\text{Sn}_{14.9}\text{Cu}_{4.5}$ Heusler alloy samples were studied using standard magnetometry methods (ZFC-FC-FH protocols) using a “Quantum Design” MPMS-7T SQUID magnetometer in a low magnetic field of 10 mT (inset in Figure 2a) and in fields of 1 T and 3 T in the wide temperature range of 2–400 K (Figure 2a). The alloy demonstrated two magnetic PTs of first and second order. The 1st-order magnetostructural PT from a ferrimagnetic (FiM) martensitic phase to an FM austenitic phase was observed at the cryogenic temperatures. The characteristic start and finish temperatures of the martensite and austenite states obtained via the tangential method are denoted as $M_S = 101$ K, $M_F = 54$ K, $A_S = 70$ K, and $A_F = 118$ K, respectively. A temperature hysteresis of about 20 K was observed during the heating/cooling process (inset in Figure 2a). The application of high magnetic fields shifted the region of the martensitic phase to lower temperatures at the rate of -2.2 K/T (Figure 2a), which made it possible to realize the inverse MCE in this alloy in relatively low magnetic fields at cryogenic temperatures. The 2nd order magnetic PT was at the Curie temperature, $T_C \approx 350$ K.

Figure 2b shows the magnetic field dependence of the magnetization of the $\text{Ni}_{45.3}\text{Mn}_{35.9}\text{Sn}_{14.3}\text{Cu}_{4.5}$ Heusler alloy at different temperatures in the vicinity of the magnetostructural PT from 50 to 130 K, with increasing and decreasing magnetic field strengths. Measurements of the field dependences of magnetization were carried out using a self-built vibrating magnetometer with a stepper motor [26] in a Bitter magnet field up to 10 T. The sample temperature was established and maintained during each measurement. Before each measurement, the sample was cooled down to 4.2 K without a magnetic field, i.e., below the M_F temperature. This was carried out to remove residual austenite phase that may have formed as a result of the previous magnetization/demagnetization processes.

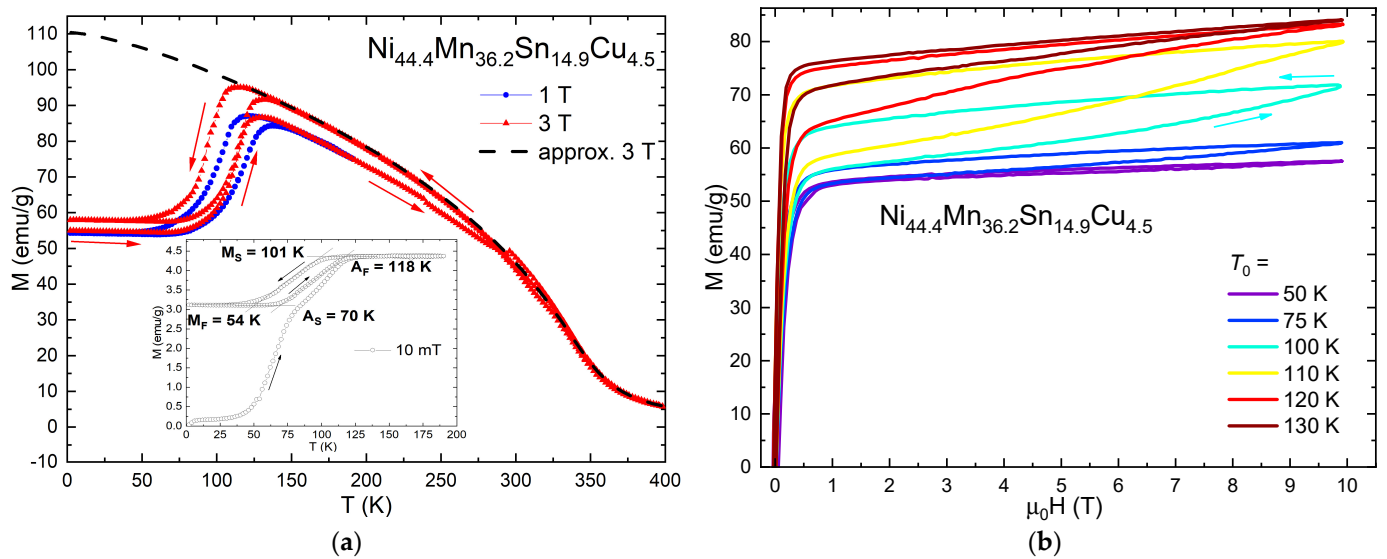


Figure 2. (a) Temperature dependences of the magnetization of the $\text{Ni}_{45.3}\text{Mn}_{35.9}\text{Sn}_{14.3}\text{Cu}_{4.5}$ Heusler alloy in high magnetic fields of 1 and 3 T (inset: in low field of 10 mT). The dashed line is the calculated curve (approximation) of the temperature dependence of the magnetization in a field of $\mu_0 H = 3$ T for the sample in austenite phase (without a magnetostructural PT). (b) Field dependences of the magnetization of the $\text{Ni}_{45.3}\text{Mn}_{35.9}\text{Sn}_{14.3}\text{Cu}_{4.5}$ Heusler alloy at different temperatures from 50 to 130 K, obtained with increasing and decreasing field strength.

2.2. Computational Methods

In order to study the role of Cu addition on the structural and magnetic properties of Ni-Mn-Sn alloy, we also carried out theoretical studies within the framework of ab initio calculations and Monte Carlo (MC) simulations.

First-principles calculations of the ground-state properties of the austenitic and martensitic phases of Cu-doped Ni-Mn-Sn alloys were performed using the projector augmented wave (PAW) method implemented in the Vienna Ab initio Simulation Package (VASP ver. 6.2) [27,28]. The generalized gradient approximation in the formulation of Perdew, Burke, and Ernzerhof [29] was chosen to calculate the exchange-correlation energy. Electron-ion interactions are described using PAW potentials with the electronic configurations as follows: $3p^6 3d^8 4s^2$ for Ni, $3p^6 3d^6 4s^1$ for Mn, $3d^{10} 4s^2 4p^2$ for Sn, and $3p^6 3d^{10} 4s^1$ for Cu. The cutoff energy of plane waves was 450 eV. The Brillouin zone was sampled using a $5 \times 5 \times 4$ mesh of k points centered at the Gamma point. The convergence criterion for the total energy was 10^{-6} eV/at. A $2 \times 2 \times 2$ supercell of 64 atoms with an 8-atom tetragonal unit cell ($L1_0$, $I4/mmm$, #139) was considered.

The geometric optimization procedure was carried out for the compounds $\text{Ni}_{32-x}\text{Cu}_x\text{Mn}_{23}\text{Sn}_9$ ($x = 1, 2, \text{ and } 3$), which correspond to $\text{Ni}_{50-x}\text{Cu}_x\text{Mn}_{35.94}\text{Sn}_{14.06}$ ($x = 1.56, 3.12 \text{ and } 4.69$ at.%), where the latter is close to the experimental $\text{Ni}_{44.4}\text{Cu}_{4.5}\text{Mn}_{36.2}\text{Sn}_{14.9}$. To form $\text{Ni}_{50-x}\text{Cu}_x\text{Mn}_{35.94}\text{Sn}_{14.06}$ ($x = 1.56, 3.12 \text{ and } 4.69$ at.%), the Mn₂ and Cu atoms were randomly distributed at Sn and Ni sites. Two magnetic configurations were considered: FM, where the Mn₁, Mn₂ and Ni magnetic moments were aligned in parallel, and FiM, where the magnetic moments of Mn₂ atoms were reversed with respect to the Mn₁ and Ni magnetic moments. Here Mn₁ and Mn₂ are Mn atoms located in the regular Mn sublattice and Sn sublattice, respectively.

The spin-polarized relativistic Korringa-Kohn-Rostoker package (SPR-KKR ver. 7.7) implemented in [30] was applied for calculation of the magnetic exchange coupling constants in the austenitic and martensitic phases of Ni-Cu-Mn-Sn. The formation of non-stoichiometric compositions was performed in the coherent potential approximation. Brillouin zone integration was performed using a special point method on a $57 \times 57 \times 57$ k-grid

(4495 k-points) to calculate self-consistent potentials and exchange interaction integrals, respectively. The energy convergence threshold was set to 0.01 mRy.

The temperature dependencies of the magnetization were modeled using the MC method, the Heisenberg Hamiltonian and Metropolis algorithm [31]. The model lattice with periodic boundary conditions consisted of 5488 atoms (for Ni₂MnSn: 2744 Ni atoms, 1372 Mn and Ga atoms) and was obtained by multiplying the 16-atom unit cell $7 \times 7 \times 7$ times. To form Ni_{50-x}Cu_xMn_{35.94}Sn_{14.06} ($x = 1.56, 3.12$ and 4.69 at.%), the Mn₂ and Cu atoms were randomly distributed at Sn and Ni sites. The number of MC steps per temperature value was 1×10^5 . To achieve thermal equilibrium in the system, the first 10^4 steps of the MC were discarded. Magnetization averaging was performed for 225 configurations for every 400 MC steps.

3. Results

3.1. Indirect MCE Estimation

The isothermal change of magnetic entropy ΔS_{iso} was obtained from Maxwell's thermodynamic relations (1) using magnetization curves with increasing field from 0 to 10 T, and is presented in Figure 2b.

$$\Delta S_{iso} = \int_0^H \left(\frac{\partial M(T, H)}{\partial T} \right)_H dH. \quad (1)$$

The maximum value of the magnetic entropy change was $\Delta S_{iso} = 9.5$ J/(kg K) at $T = 113$ K in $\mu_0 H = 10$ T (Figure 3a). The ΔS_{iso} values obtained in the vicinity of the hysteresis of the magnetostructural PT are irreversible because reversible MCE values in this region can be obtained by demagnetizing the sample or by turning the magnetic field on again.

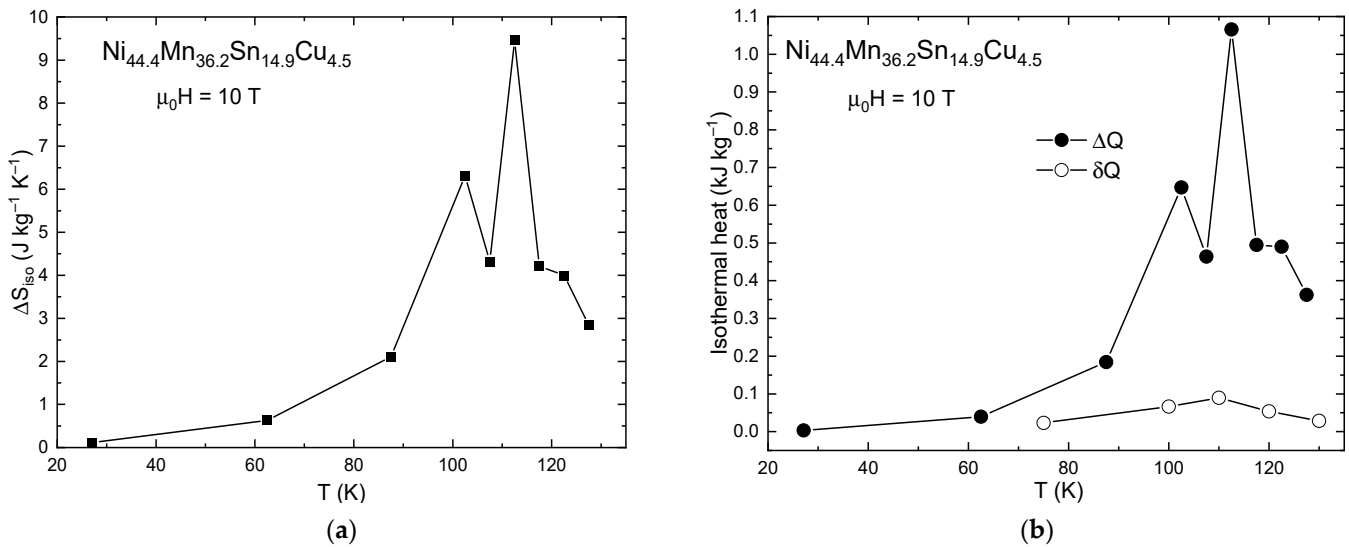


Figure 3. (a) Temperature dependence of the isothermal entropy changes ΔS_{iso} in the magnetic field $\mu_0 H = 10$ T for the Heusler Ni_{44.4}Mn_{36.2}Sn_{14.9}Cu_{4.5} alloy. (b) Temperature dependences of the isothermal heat ΔQ and the irreversible magnetization losses δQ in $\mu_0 H = 10$ T for the Heusler Ni_{44.4}Mn_{36.2}Sn_{14.9}Cu_{4.5} alloy.

The isothermal heat ΔQ is also an important parameter of the working body of a magnetic refrigerator; it allows one to estimate the amount of heat that can be taken from a cooled bath as a result of one ideal cycle of isothermal magnetization/demagnetization processes. Figure 3b shows the ΔQ values calculated from the ΔS_{iso} values using Equation (2):

$$\Delta Q = -T\Delta S_{iso}. \quad (2)$$

The maximum value was $\Delta Q = 1.06$ kJ/kg at $T = 113$ K in a magnetic field of 10 T, which is an order of magnitude lower than the maximum known value for MnAs at room temperature in the same magnetic field [32].

The presence of field hysteresis (Figure 2a) in the vicinity of the magnetostructural PT in the sample's magnetization/demagnetization cycle leads to irreversible heat release δQ , which was calculated using Equation (3):

$$\delta Q = \mu_0 \oint H dM. \quad (3)$$

Figure 3b shows the δQ values calculated for different temperatures with the maximal value $\delta Q = 0.09$ kJ/kg at $T = 110$ K. This value is only 8.5% of the maximal ΔQ value, which makes the Heusler $\text{Ni}_{44.4}\text{Mn}_{36.2}\text{Sn}_{14.9}\text{Cu}_{4.5}$ alloy interesting for use as a magnetocaloric working body in the temperature range of natural gas liquefaction [2], despite the presence of field hysteresis in the magnetostructural PT.

3.2. Direct MCE Measurements

The extraction method in a Bitter magnet field of up to 10 T was used for direct measurement of the MCE in the Heusler $\text{Ni}_{44.4}\text{Mn}_{36.2}\text{Sn}_{14.9}\text{Cu}_{4.5}$ alloy under adiabatic conditions ΔT_{ad} . This method was described in detail in [33]. The Bitter magnet produced a steady magnetic field. The temperature change of the sample due to MCE was measured using a differential chromel–gold thermocouple with an accuracy of 0.05 K. The temperature was controlled using a Lake Shore thermo-controller. The sample was placed within a thermal screen to minimize heat exchange with the environment. Movement of the sample to and from the region of the maximum magnetic field was forced with the help of a special actuator. The sample was moved for a duration of 1 s from the center of the Bitter magnet to the outside (or vice versa) at a distance of 35 cm. It should be noted that the magnetic field values before magnetization and after demagnetization were less than 2% of the maximum field in the center of the Bitter coil.

The studies were carried out in two different regimes: (1) sequential heating of the sample, (2) thermal cycling of the sample. In the first case, the sample temperature was successively raised and ΔT_{ad} was measured at selected temperatures. In the second case, the sample was pre-cooled to 4.2 K, and then its temperature was raised to the required temperature for measurement. Figure 4 shows the results of measurements of the ΔT_{ad} value in magnetic fields of 1.8 T and 10 T: closed circles indicate sequential heating and open circles indicate thermal cycling. The inverse MCE was observed in the low-temperature region in a field of 1.8 T in both measurement regimes (Figure 4). The maximum value of the inverse MCE in a field of 1.8 T was observed in the vicinity of the 1st order PT, with a value of $\Delta T_{\text{ad}} = -0.5$ K at an initial temperature $T_0 = 117$ K (Figure 4). The inverse MCE increased with increasing magnetic field up to 10 T, reaching $\Delta T_{\text{ad}} = -2.7$ K at $T_0 = 117$ K (Figure 4). It is interesting that direct MCE in a magnetic field of 10 T was observed in the FiM martensite phase and reached $\Delta T_{\text{ad}} = 0.7$ K (Figure 4) in the sequential heating regime in the temperature range of 20–60 K.

3.3. Computational Results

We will now discuss the results of the geometric optimization of the crystal structures of the austenitic and martensitic phases as well as the calculation of the magnetic properties of Heusler $\text{Ni}_{50-x}\text{Cu}_x\text{Mn}_{35.94}\text{Sn}_{14.06}$ alloys.

Figure 5 shows the energy landscape $E(c/a)$ of $\text{Ni}_{50-x}\text{Cu}_x\text{Mn}_{35.94}\text{Sn}_{14.06}$, including the response to volume-conserving elongations and compressions of the cubic $L2_1$ structure along the c axis. The results are shown for both FM and FiM solutions (Figure 5a). It can be seen that the FM solution exhibits only one global cubic minimum at $c/a = 1$, which is 11 meV/atom higher in energy than observed for FiM, indicating an instability of the FM tetragonal phase. For all compounds, the FiM ordering was energetically preferable to

the FM ordering for both cubic austenitic and tetragonal martensitic phases. The global minimum for the FiM tetragonal phase took place at around $c/a = 1.25$.

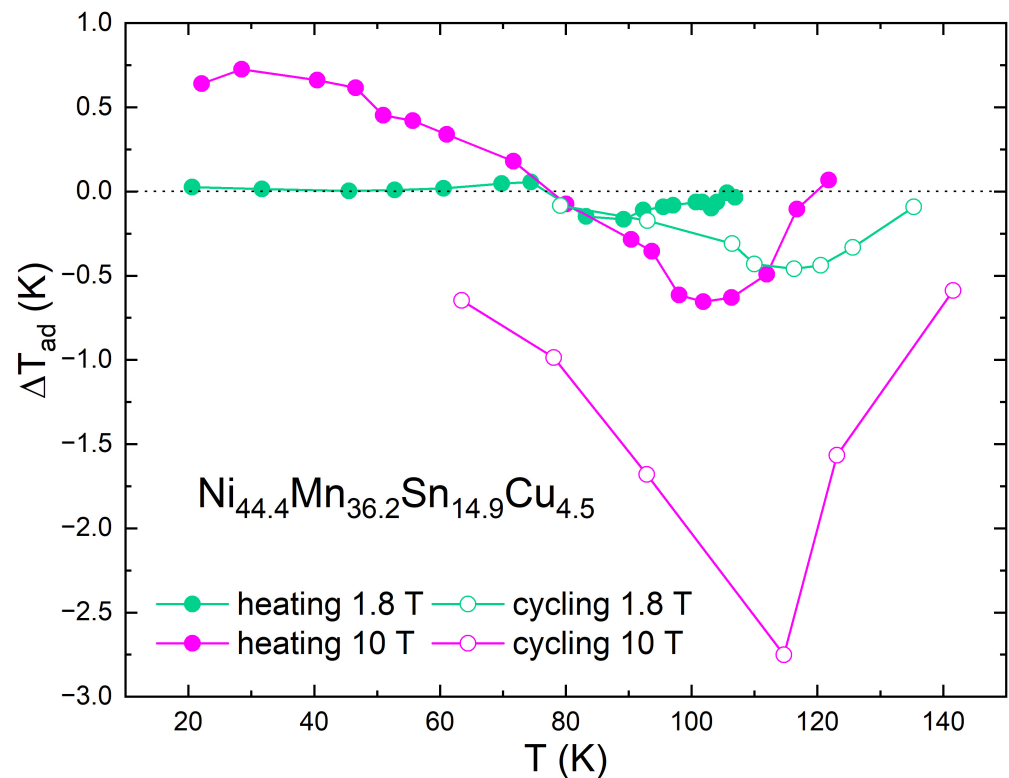


Figure 4. Temperature dependences of the adiabatic temperature change ΔT_{ad} for the $\text{Ni}_{44.4}\text{Mn}_{36.2}\text{Sn}_{14.9}\text{Cu}_{4.5}$ Heusler alloy, measured in magnetic fields of 1.8 T (green curves) and 10 T (violet curves) in two different regimes: solid circles—during sequential heating of the sample; open circles—after pre-cooling down to 4.2 K and subsequent heating to the measurement temperature.

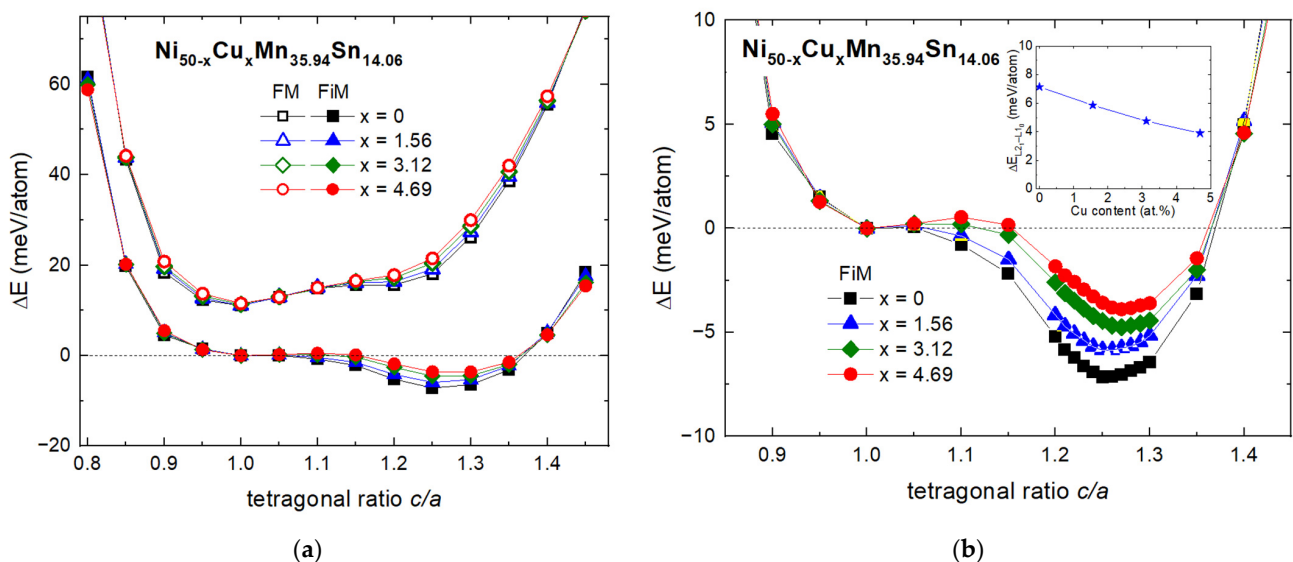


Figure 5. (a) Energy difference as a function of the tetragonal c/a ratio for $\text{Ni}_{50-x}\text{Cu}_x\text{Mn}_{35.94}\text{Sn}_{14.06}$ ($x = 0, 1.56, 3.12,$ and 4.69). For all compounds, the zero energy corresponds to the FiM cubic structure. Filled and open symbols denote the FiM and FM solutions, respectively. (b) Enlarged scale for the FiM solution. The inset shows the energy difference between FiM cubic and tetragonal phases as a function of Cu content.

A close look at the FiM $E(c/a)$ curves shown in Figure 5b reveals that the c/a ratio of the tetragonal phase varied slightly from 1.25 to 1.27 with increasing Cu content due to a reduction (increase) in the tetragonal lattice constant a_t (c), respectively (see Table 1). In addition, the optimized cubic lattice constant increased slightly with the addition of Cu. This is explained by the slightly larger atomic radius of Cu ($r = 1.28 \text{ \AA}$) compared to that of Ni ($r = 1.24 \text{ \AA}$). It should be noted that partial substitution of Ni with Cu revealed an almost linear decrease in the energy difference ($\Delta E_{L2_1-L1_0}$) between the FiM cubic and tetragonal structure, as is evident from Figure 5b. For the parent compound with $x = 0$, $\Delta E_{L2_1-L1_0}$ was calculated to be 7.145 meV/atom, whereas in the case of $x = 4.69$ at.%, it reduced to 3.89 meV/atom. The decrease in the energy barrier with the Cu content indirectly indicates the reduction in the martensitic transition temperature T_m . The T_m temperature can be estimated from a rough approximation: $\Delta E_{L2_1-L1_0} \approx k_B T_m$, where k_B is the Boltzmann constant. According to this expression, $T_m \approx 83 \text{ K}$ for $\text{Ni}_{50}\text{Mn}_{35.94}\text{Sn}_{14.06}$ and 45 K for $\text{Ni}_{45.31}\text{Cu}_{4.69}\text{Mn}_{35.94}\text{Sn}_{14.06}$.

Table 1. Optimized lattice parameters and Debye temperatures of cubic and tetragonal structures of $\text{Ni}_{50-x}\text{Cu}_x\text{Mn}_{35.94}\text{Sn}_{14.06}$. The Debye temperatures were calculated from elastic moduli.

Phase	Parameters	$x = 0$	$x = 1.56$	$x = 3.12$	$x = 4.69$
FiM cubic ($c/a = 1$)	a_0 (\AA)	5.953	5.955	5.959	5.963
	Θ_D (K)	316	308	293	282
FiM tetragonal ($c/a = 1.27$)	a_t (\AA)	5.526	5.513	5.502	5.500
	c (\AA)	6.908	6.947	6.988	6.994
	c/a	1.25	1.26	1.27	1.27
	Θ_D (K)	333	325	308	295

A more correct way to estimate the martensitic transition temperature is to calculate the free energies of the austenitic and martensitic phases. For simplicity of calculation, we only considered the lattice contribution to the free energy, which at low temperatures plays a predominant role compared to the electronic and magnetic contributions:

$$F(T, V) = E(V) + F_{lat}(T, V), \quad (4)$$

where $E(V)$ is the ground-state energy calculated at $T = 0 \text{ K}$, and $F_{lat}(T, V)$ is the lattice contribution calculated within the Debye model [34].

In Figure 6, we illustrate the free energies of $L2_1$ cubic and $L1_0$ tetragonal phases as well as the free-energy difference $\Delta F = F_{L2_1} - F_{L1_0}$ for the $\text{Ni}_{45.31}\text{Cu}_{4.69}\text{Mn}_{35.94}\text{Sn}_{14.06}$ alloy as an example. For $\Delta F > 0$, the $L1_0$ phase (martensite) is preferable and, vice versa, the $L2_1$ phase (austenite) is stable for $\Delta F < 0$. As is evident from the figure, both free-energy curves reveal a non-linear behavior with temperature and intersect with each other at low temperatures. The martensitic transition temperature extracted from $\Delta F = 0$ is about 88 K, which agrees well with the experimental value (85.75 K) for $\text{Ni}_{44.4}\text{Mn}_{36.2}\text{Sn}_{14.9}\text{Cu}_{4.5}$, where T_m was computed via $T_m = (M_s + M_f + A_f + A_s)/4$. The low T_m temperature suggests that the zero-point vibrational energy ($\frac{9}{8}k_B\Theta_D$) plays a predominant role as compared to a vibrational entropy in the F_{lat} term. Thus, T_m is mainly contributed by $\Delta E_{L2_1-L1_0}$ at $T = 0 \text{ K}$ and $\Delta\Theta_D^{L2_1-L1_0}$ at $T > 0 \text{ K}$. For $\text{Ni}_{45.31}\text{Cu}_{4.69}\text{Mn}_{35.94}\text{Sn}_{14.06}$, $\Delta\Theta_D^{L2_1-L1_0}$ is 13 K in absolute value. We would like to note that T_m is sensitive to $\Delta\Theta_D^{L2_1-L1_0}$, and an increase in $\Delta\Theta_D^{L2_1-L1_0}$ ($\Theta_D^{L2_1} < \Theta_D^{L1_0}$) leads to a reduction in T_m ; the austenitic phase becomes stable in the whole temperature range at a $\Delta\Theta_D^{L2_1-L1_0}$ of about 30 K in absolute value. On the other hand, an increase in $\Delta\Theta_D^{L2_1-L1_0}$ ($\Theta_D^{L2_1} > \Theta_D^{L1_0}$) shifts T_m to higher temperatures.

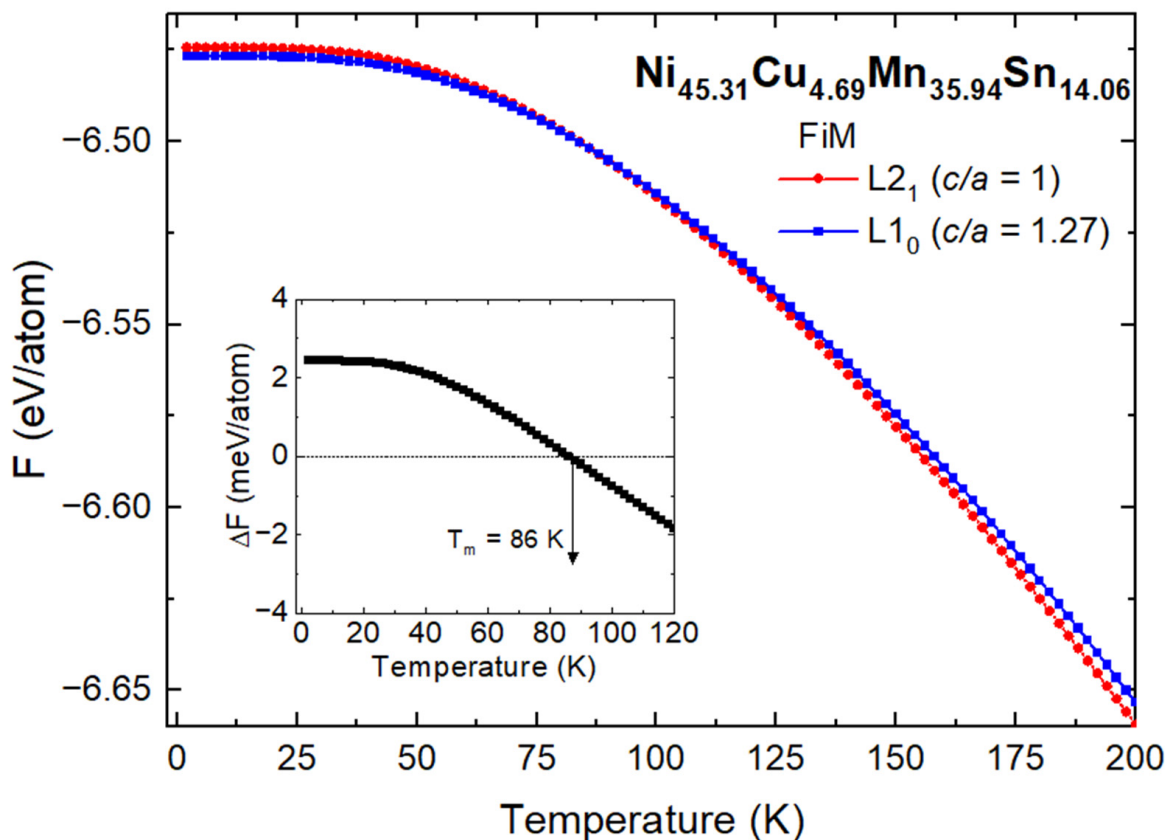


Figure 6. Temperature dependencies of the free energy of cubic and tetragonal phases of $\text{Ni}_{45.31}\text{Cu}_{4.69}\text{Mn}_{35.94}\text{Sn}_{14.06}$. The inset shows the free-energy difference between $L2_1$ and $L1_0$ structures.

Figure 7 shows the pairwise exchange coupling constants J_{ij} as function of the distance between i and j atoms for FiM- $L2_1$ and FiM- $L1_0$ $\text{Ni}_{45.31}\text{Cu}_{4.69}\text{Mn}_{35.94}\text{Sn}_{14.06}$ alloy as an example. The magnetic interactions reveal a similar behavior for all compounds under study because Cu atoms are nonmagnetic. For both phases, intra-sublattice J_{ij} constants between Mn atoms (Mn_1 - Mn_1 and Mn_2 - Mn_2) show similar damped oscillatory behavior as a function of the distance between atoms up to $d/a \approx 2$, with the exception of the interactions for the three coordination shells of cubic structure. In this case, J_{ij} (Mn_1 - Mn_1) demonstrates a reducing FM character, whereas J_{ij} (Mn_2 - Mn_2) within the first and second coordination shells exhibits a reducing AFM character.

The cubic inter-sublattice interactions between the nearest Mn_1 - Mn_2 atoms located at a smaller distance ($d/a = 0.5$) compared to the nearest pairs $\text{Mn}_{1(2)}$ - $\text{Mn}_{1(2)}$ ($d/a = \sqrt{2}/2$) are characterized by a strong AFM interaction, which gradually decreases with increasing d/a . In contrast to the cubic structure, the strongest AFM exchange (≈ -20 meV) between the four nearest atoms Mn_1 - Mn_2 located in the (110) plane is found for the tetragonal structure due to the smallest distance ($d/a = 0.5$), whereas the two next nearest atoms Mn_1 - Mn_2 ($d/a \approx 0.627$) exhibit a strong ferromagnetic interaction with $J_{ij} \approx 11.5$ meV. The $\text{Mn}_{1(2)}$ -Ni interactions show a similar behavior for both phases, demonstrating the FM exchange only between the nearest neighbors. Generally, the behavior of J_{ij} coupling constants is similar to those that were previously reported for Ni-Mn-Sn alloys [35].

Let us make a general remark concerning the behavior of the exchange interaction parameters for the remaining compounds in the cubic and tetragonal phases. Since the substitution of Ni with Cu influences a small change in the crystal structure parameters for both phases, it will also weakly affect the exchange constants between the nearest pairs of Mn_1 -Ni and Mn_2 -Ni (see Table 2). For the cubic structure, a slight enhancement of the FM interactions $J_{\text{Mn}_{1(2)}-\text{Mn}_{1(2)}}$ and $J_{\text{Mn}_{1(2)}-\text{Ni}}$ and a weakening of the AFM interaction $J_{\text{Mn}_1-\text{Mn}_2}$ with increasing Cu content is observed, which also affects the Curie temperature

of austenite (T_C^A). In the case of the tetragonal structure, a weakening of FM and AFM interactions between Ni, Mn₁ and Mn₂ atoms is observed. However, the Curie temperature of martensite, T_C^M , increases similarly to T_C^A . The increase in T_C^M is caused by the weakening of the strong AFM interaction between the nearest Mn₁-Mn₂, the change of which has a larger contribution to the magnetic energy compared to the change of $J_{Mn1(2)-Mn1(2)}$ and $J_{Mn1(2)-Ni}$ interactions as a function of Cu content.

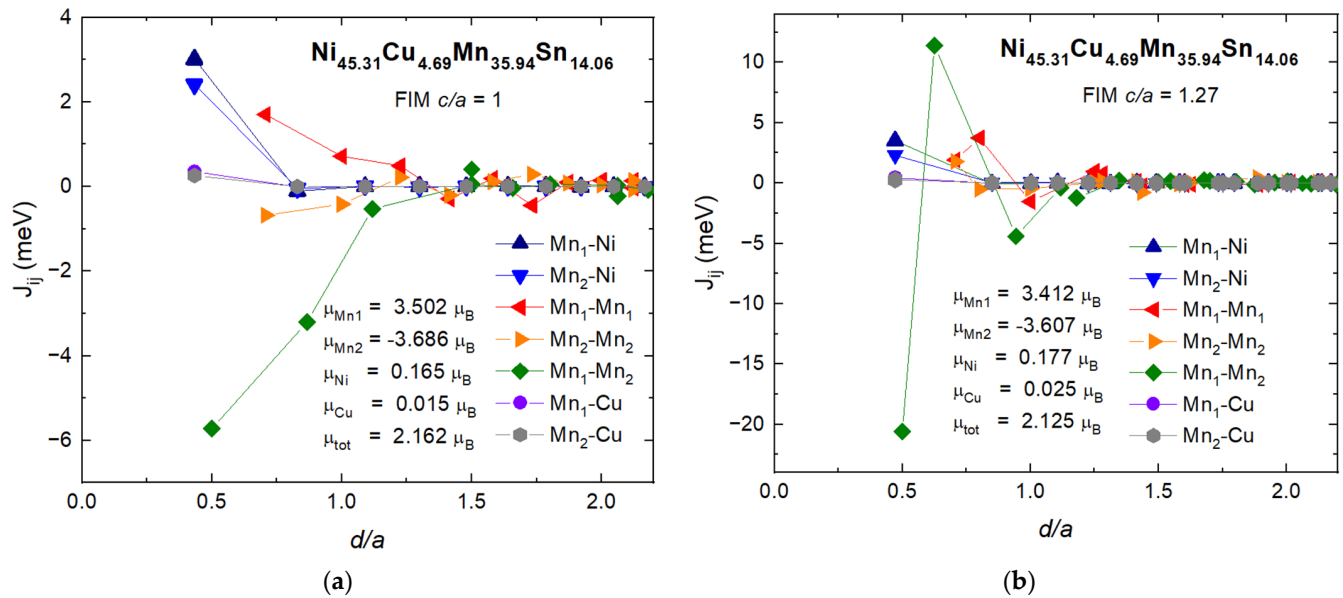


Figure 7. Calculated magnetic exchange parameters of (a) FiM L21- and (b) L10-Ni_{45.31}Cu_{4.69}Mn_{35.94}Sn_{14.06} as functions of the distance between the atoms in units of the lattice constant a . Positive J_{ij} values denote FM interactions, and negative ones denote AFM interactions.

Table 2. The nearest exchange coupling constants and Curie temperatures calculated within the MC method and MFA for cubic and tetragonal structures of Heusler Ni_{50-x}Cu_xMn_{35.94}Sn_{14.06} alloys.

x	Mn ₁ -Ni	Mn ₂ -Ni	Mn ₁ -Mn ₁	Mn ₂ -Mn ₂	Mn ₁ -Mn ₂	T_C (MC)	T_C (MFA)
FiM cubic structure							
0	2.961	2.341	1.082	-0.936	-6.065	425	423.4
1.56	2.977	2.364	1.201	-0.837	-5.925	430	433.5
3.12	2.988	2.384	1.492	-0.772	-5.859	452	444.8
4.69	2.999	2.402	1.702	-0.678	-5.722	464	453.1
FiM tetragonal structure							
0	3.514	2.308	2.035	1.859	-21.902	484	544.9
1.56	3.502	2.299	1.985	1.826	-21.513	506	547.5
3.12	3.495	2.294	1.942	1.798	-21.071	514	549.6
4.69	3.489	2.287	1.906	1.779	-20.598	523	551.4

Figure 8a shows the $T-x$ phase diagram for Ni_{50-x}Cu_xMn_{35.94}Sn_{14.06}, including the predicted T_m and T_C temperatures and the experimentally measured values of T_m and T_C^A . With increasing Cu doping level, T_m reduces nonlinearly from 133 K ($x = 0$ at.%) to 88 K ($x = 4.69$ at.%). This is mainly due to a decrease in the energy barrier $\Delta E_{L21-L10}$ and $\Delta \Theta_D^{L21-L10}$, both of which have maxima at $x = 0$ (see Figure 5 and Table 1). The predicted value of T_m for Ni_{45.31}Cu_{4.69}Mn_{35.94}Sn_{14.06} is close to the experimental one for Ni_{44.4}Cu_{4.5}Mn_{36.2}Sn_{14.9}. As for the Curie temperature, MC simulations and mean-field approximation (MFA) show a similar T_C^A trend with the increase in Cu content. Nevertheless, the experimental value of T_C^A for Ni_{44.4}Cu_{4.5}Mn_{36.2}Sn_{14.9} is less than the theoretical one by about 100 K.

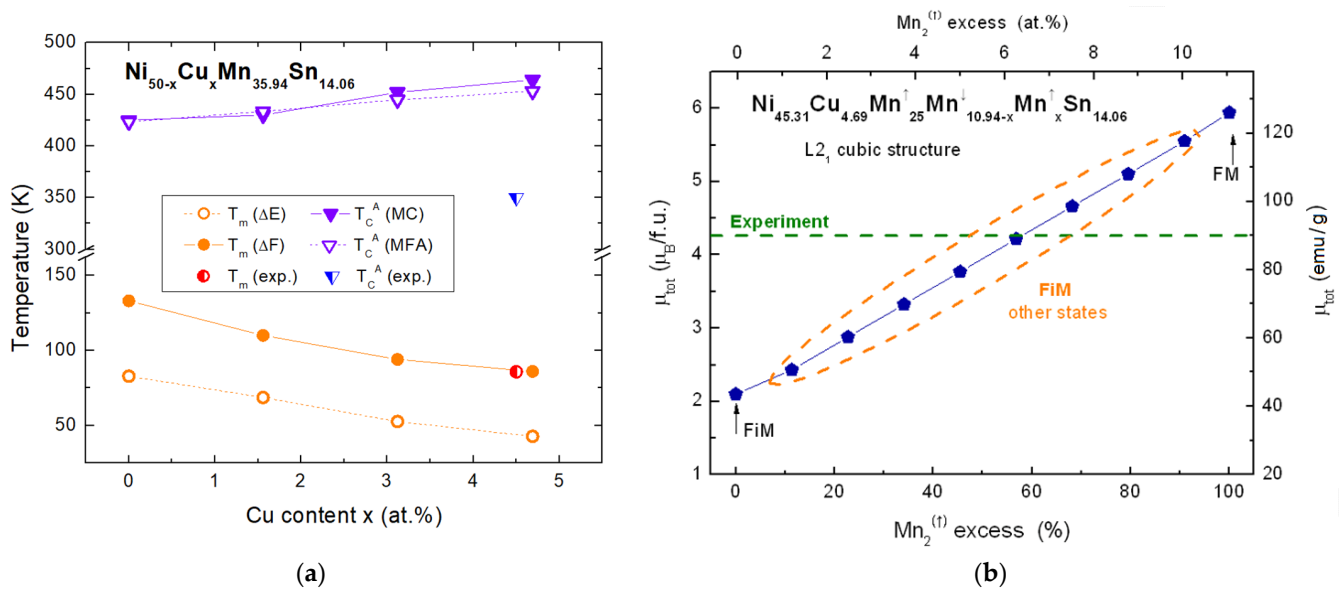


Figure 8. (a) Calculated phase diagram for $\text{Ni}_{50-x}\text{Cu}_x\text{Mn}_{35.94}\text{Sn}_{14.06}$ ($x = 0, 1.56, 3.12$ and 4.69). Here, $T_m(\Delta E)$ and $T_m(\Delta F)$ are the martensitic transformation temperatures calculated from the energy difference at $T = 0$ K, which has been converted to a temperature scale, and from the free-energy difference considering only lattice contribution, respectively; T_C^A is the Curie temperatures of austenite calculated by MC and MFA methods. The experimental values of T_m and T_C^A refer to $\text{Ni}_{44.4}\text{Mn}_{36.2}\text{Sn}_{14.9}\text{Cu}_{4.5}$, and T_m is computed via $T_m = (M_s + M_f + A_f + A_s)/4$. (b) The calculated total magnetic moment (filled symbols) of $\text{Ni}_{45.31}\text{Cu}_{4.69}\text{Mn}_{35.94}\text{Sn}_{14.06}$ with the cubic structure as a function of Mn_2 atoms at Sn sites with a parallel magnetic moment to that of Mn_1 atoms. The experimental magnetization for the austenitic phase of $\text{Ni}_{44.4}\text{Mn}_{36.2}\text{Sn}_{14.9}\text{Cu}_{4.5}$ is highlighted with the green dashed line.

4. Discussion

Let us next discuss the calculated total magnetic moment μ_{tot} for $\text{Ni}_{45.31}\text{Cu}_{4.69}\text{Mn}_{35.94}\text{Sn}_{14.06}$ and its relation to the experimentally obtained moment for $\text{Ni}_{44.4}\text{Cu}_{4.5}\text{Mn}_{36.2}\text{Sn}_{14.9}$. It follows from Figure 6 that the magnetic reference state for both austenite and martensite is an FiM one, where all magnetic moments of Mn_1^{\uparrow} and Mn_2^{\downarrow} are oppositely aligned. As a consequence, the μ_{tot} is calculated to be almost equal 2.16 and $2.12 \mu_B$ or 45.6 and 44.8 emu/g, respectively. The latter value is close to the experimental magnetization of martensite (≈ 53 emu/g). However, there is some discrepancy between the calculated and measured values of μ_{tot} for austenite. The experiment yielded a μ_{tot} value that was double the calculated value (90 emu/g—dashed line in Figure 8b). On the other hand, the calculated value of μ_{tot} for FM austenite, which is energetically unfavorable, is about $5.94 \mu_B$ or 125.6 emu/g larger than the experimental one. The dashed line in Figure 2a is the calculated curve (approximation) of the temperature dependence of the magnetization in $\mu_0 H = 3$ T for the sample in the austenite phase without a magnetostructural PT. This curve was calculated using the approach proposed in [36]. The magnetization value obtained using this approach is 110 emu/g (Figure 2a). This is the estimation of the maximal magnetization of the austenitic phase “without martensitic transition”, and it is very close to the calculated value.

To explain the observed discrepancy, we suggest that not all Mn_2 atoms located at the Sn sublattice have an antiparallel magnetic moment with respect to Mn_1 atoms located at the regular Mn sublattice. To prove this, we additionally performed CPA calculations of μ_{tot} for $\text{L2}_1\text{-Ni}_{45.31}\text{Cu}_{4.69}\text{Mn}_{35.94}\text{Sn}_{14.06}$ (or $\text{Ni}_{45.31}\text{Cu}_{4.69}\text{Mn}_{25}^{\uparrow}\text{Mn}_{10.94-x}^{\downarrow}\text{Mn}_x^{\uparrow}\text{Sn}_{14.06}$) using SPR-KKR code as a function of Mn_2 atoms at Sn sites with a parallel magnetic moment to that of Mn_1 atoms, as shown in Figure 8b. As can be seen from the figure, μ_{tot} increases linearly with the fraction of Mn_2^{\uparrow} atoms and reaches $5.94 \mu_B$ or 125.6 emu/g for 100% of the Mn_2^{\uparrow} spins aligned parallel to the Mn_1^{\uparrow} ones (FM order). We found that the experimental

value of μ_{tot} can be reached theoretically if only $\approx 40\%$ of the Mn_2 atoms interact antiferromagnetically with the Mn_1 atoms. This finding allows us to conclude that the experimental sample had some kind of FiM order, with a predominance of FM-ordered Mn atoms.

The inverse MCE at low temperatures in the Heusler $Ni_{33.7}Co_{14.8}Mn_{35.4}Ti_{16.1}$ alloy showed similar values at low temperatures [23]: maximal $\Delta T_{ad} = -2.7$ K at $T_0 = 90$ K in a magnetic field of 20 T. This may be a physical limit on the value of the inverse MCE for Heusler alloys with PTs at low temperatures, which is significantly lower than in known Heusler alloys with the inverse MCE at room temperature, for example [37]. The further study of medium-entropy [38–40] and high-entropy [41–43] alloys that do not contain rare-earth elements will reveal compositions with high inverse MCE for application in low-temperature SMC.

5. Conclusions

The inverse MCE in a Heusler $Ni_{44.4}Mn_{36.2}Sn_{14.9}Cu_{4.5}$ alloy in the low-temperature region was observed in a magnetic field of 1.8 T in both measurement regimes: sequential heating and thermal cycling. The maximum value of the inverse MCE in the vicinity of the first-order PT in a magnetic field of 1.8 T was observed to be $\Delta T_{ad} = -0.5$ K at an initial temperature $T_0 = 117$ K. The inverse MCE reached up to $\Delta T_{ad} = -2.7$ K at $T_0 = 117$ K with the increase in the magnetic field up to 10 T. The direct MCE in the FiM martensite phase was observed in a magnetic field of 10 T and reached the maximal value of $\Delta T_{ad} = 0.7$ K in the sequential heating regime in the temperature range of 20–60 K.

First-principles and MC approaches were applied to determine the phase diagram for FM-ordered $Ni_{50-x}Cu_xMn_{35.94}Sn_{14.06}$ ($x = 0, 1.56, 3.12$ and 4.69) compounds, which were similar in composition to the experimental sample. Cu doping led to a decrease in the T_m temperature and an increase in the T_C^A temperature. This was mainly due to the slight change in the optimized lattice constants, magnetic exchange interactions and Debye temperatures for austenite and martensite. From the analysis of our computational results, we suggest that the experimental sample exhibited some type of FiM order in the austenite, with a predominance of ferromagnetically ordered Mn atoms. This theory was satisfactorily confirmed by our experiment, which will make it possible to predict the transition temperatures, magnetizations and MCE properties of Heusler Ni-Mn-Sn family alloys when a portion of the Sn atoms are replaced with Cu.

Author Contributions: Conceptualization, A.P.K. and V.G.S.; Methodology, Y.S.K. and V.D.B.; Software, V.V.S.; Formal analysis, A.P.K., Y.S.K. and V.V.S.; Investigation, Y.S.K., A.V.K., R.Y.G., I.I.M. and V.V.S.; Resources, A.V.M. and J.Č.; Writing—original draft, A.P.K., Y.S.K. and V.V.S.; Supervision, V.D.B. and V.G.S.; Project administration, V.G.S. All authors of the manuscript contributed equally to data acquisition and analysis, writing, editing and formatting. All authors have read and agreed to the published version of the manuscript.

Funding: The magnetization and magnetocaloric measurements were carried out within the framework of Russian Science Foundation project № 20-19-00745, <https://rscf.ru/project/20-19-00745/> (accessed on 1 December 2023). The alloy preparation and structure analysis were carried out by R.Y.G and I.I.M. within the framework of the state task of IMSP RAS. V.V.S. the financial support from the Priority-2030 Program of NUST “MISiS” (grant No. K2-2022-022) (the total energy calculations). V.D.B. acknowledges the Ministry of Science and Higher Education of the Russian Federation within the Russian State Assignment, under Contract 075-01493-23-00 (the phonon calculations).

Data Availability Statement: The data presented in this study are openly available in Preprints.org at <https://doi.org/10.20944/preprints202310.0715.v1>.

Conflicts of Interest: The authors declare no conflict of interest.

References

1. Giaouque, W.F.; MacDougall, D.P. Attainment of Temperatures Below 1 Absolute by Demagnetization of $Gd_2(SO_4)_3 \cdot 8H_2O$. *Phys. Rev.* **1933**, *43*, 768. [[CrossRef](#)]
2. Koshkid'ko, Y.S.; Dilmieva, E.T.; Kamantsev, A.P.; Mashirov, A.V.; Cwik, J.; Kol'chugina, N.B.; Koledov, V.V.; Shavrov, V.G. Magnetocaloric Materials for Low-Temperature Magnetic Cooling. *J. Commun. Technol. Electron.* **2023**, *68*, 379–388. [[CrossRef](#)]
3. Tishin, A.M.; Spichkin, Y.I. *The Magnetocaloric Effect and Its Applications*; IOP Publisher: Bristol, UK, 2003; p. 476.
4. Belov, K.P. *The Magnetothermal Phenomena in Rare-Earth Magnetics*; Nauka: Moscow, Russia, 1990.
5. Khovaylo, V.V.; Taskaev, S.V. Magnetic Refrigeration: From Theory to Applications. *Encycl. Smart Mater.* **2022**, *5*, 407–417.
6. Tang, X.; Sepehri-Amin, H.; Terada, N.; Martin-Cid, A.; Kurniawan, I.; Kobayashi, S.; Kotani, Y.; Takeya, H.; Lai, J.; Matsushita, Y.; et al. Magnetic refrigeration material operating at a full temperature range required for hydrogen liquefaction. *Nat. Commun.* **2022**, *13*, 1817. [[CrossRef](#)] [[PubMed](#)]
7. Aziz, M. Liquid Hydrogen: A Review on Liquefaction, Storage, Transportation, and Safety. *Energies* **2021**, *14*, 5917. [[CrossRef](#)]
8. Zhang, H.; Sun, Y.J.; Niu, E.; Yang, L.H.; Shen, J.; Hu, F.X.; Sun, J.R.; Shen, B.G. Large magnetocaloric effects of $RFeSi$ ($R = Tb$ and Dy) compounds for magnetic refrigeration in nitrogen and natural gas liquefaction. *Appl. Phys. Lett.* **2013**, *103*, 202412. [[CrossRef](#)]
9. Timmerhaus, K.D.; Reed, R.P. *Cryogenic Engineering: Fifty Years of Progress*; Springer Science & Business Media: New York, NY, USA, 2007.
10. Andreenko, A.S.; Belov, K.P.; Nikitin, S.A.; Tishin, A.M. Magnetocaloric effects in rare-earth magnetic materials. *Sov. Phys. Usp.* **1989**, *32*, 649–664. [[CrossRef](#)]
11. Zheng, X.Q.; Xu, Z.Y.; Zhang, B.; Hu, F.X.; Shen, B.G. The normal and inverse magnetocaloric effect in RCu_2 ($RB = Tb, Dy, Ho, Er$) compounds. *J. Magn. Magn. Mater.* **2017**, *421*, 448–452. [[CrossRef](#)]
12. Kuchin, A.G.; Iwasieczko, W.; Platonov, S.P. The magnetocaloric effect in R_2Fe_{17} intermetallics with different types of magnetic phase transition. *Low Temp. Phys.* **2015**, *41*, 985–989. [[CrossRef](#)]
13. Kamantsev, A.P.; Koshkidko, Y.S.; Taskaev, S.V.; Khovaylo, V.V.; Koshelev, A.V.; Cwik, J.; Shavrov, V.G. Inverse Magnetocaloric Effect and Kinetic Arrest Behavior in As-Cast Gd_2In at Cryogenic Temperatures. *J. Supercond. Nov. Magn.* **2022**, *35*, 2181–2186. [[CrossRef](#)]
14. Kuchin, A.G.; Platonov, S.P.; Mukhachev, R.D.; Lukoyanov, A.V.; Volegov, A.S.; Gaviko, V.S.; Yakovleva, M.Y. Large Magnetic Entropy Change in $GdRuSi$ Optimal for Magnetocaloric Liquefaction of Nitrogen. *Metals* **2023**, *13*, 290. [[CrossRef](#)]
15. Nikitin, S.A.; Skokov, K.P.; Koshkid'ko, Y.S.; Pastushenkov, Y.G.; Ivanova, T.I. Giant Rotating Magnetocaloric Effect in the Region of Spin-Reorientation Transition in the $NdCo_5$ Single Crystal. *Phys. Rev. Lett.* **2010**, *105*, 137205. [[CrossRef](#)] [[PubMed](#)]
16. Moon, J.Y.; Kim, M.K.; Oh, D.G.; Kim, J.H.; Shin, H.J.; Choi, Y.J.; Lee, N. Anisotropic magnetic properties and giant rotating magnetocaloric effect in double-perovskite Tb_2CoMnO_6 . *Phys. Rev. B* **2018**, *98*, 174424. [[CrossRef](#)]
17. Koshkid'ko, Y.; Cwik, J.; Dilmieva, E.; Pandey, S.; Quetz, A.; Aryal, A.; Dubenko, I.; Ali, N.; Granovsky, A.; Lähderanta, E.; et al. Inverse magnetocaloric effects in metamagnetic Ni-Mn-In-based alloys in high magnetic fields. *J. Alloys Compd.* **2017**, *695*, 3348–3352. [[CrossRef](#)]
18. Konoplyuk, S.M.; Kokorin, V.V.; Mashirov, A.V.; Kamantsev, A.P.; Koledov, V.V.; Shavrov, V.G.; Koshelev, A.V. Direct measurements of adiabatic temperature change in $Ni_{49.9}Mn_{37.03}Sb_{12.3}Fe_{0.77}$ alloy due to magnetocaloric effect in the temperature range of martensitic transformation. *IEEE Trans. Magn.* **2018**, *54*, 2500204. [[CrossRef](#)]
19. Sokolovskiy, V.V.; Nachinova, D.V.; Buchel'nikov, V.D.; Dilmieva, E.T.; Koshkidko, Y.S.; Emelyanova, S.M.; Marchenkova, E.B.; Marchenkov, V.V. Magnetic and magnetocaloric properties of Heusler alloys Ni-Mn-Sn with an excess of Mn within the theoretical-land experimental approaches. *Chel. Phys.-Math. J.* **2020**, *5*, 493–503. [[CrossRef](#)]
20. Lekkla, P.; Jantaratana, P.; Chotibhawaris, T. Magnetocaloric Effect in CoFe-Electroplated $Ni_{50}Mn_{33}In_{16}Cr_1$ Alloy. *Metals* **2022**, *12*, 2137. [[CrossRef](#)]
21. Dadda, K.; Alleg, S.; Souilah, S.; Daza, J.; Saurina, J.; Suñol, J.-J.; Bessais, L.; Hlil, E.-K. Microstructure, Critical Behavior and Magnetocaloric Properties of Melt-Spun $Ni_{51.82}Mn_{32.37}In_{15.81}$. *Magnetochemistry* **2022**, *8*, 179. [[CrossRef](#)]
22. Marchenkov, V.V.; Emelyanova, S.M.; Marchenkova, E.B. Martensitic Transformation Temperatures and Hall Effect in $Ni_{47-x}Mn_{41+x}In_{12}$ ($x = 0, 1, 2$) Alloys. *Materials* **2023**, *16*, 672. [[CrossRef](#)]
23. Beckmann, B.; Koch, D.; Pfeuffer, L.; Gottschall, T.; Taubel, A.; Adabifiroozjaei, E.; Miroshkina, O.N.; Riegg, S.; Niehoff, T.; Kani, N.A.; et al. Dissipation losses limiting first-order phase transition materials in cryogenic caloric cooling: A case study on all-d-metal Ni (-Co)-Mn-Ti Heusler alloys. *Acta Mater.* **2023**, *246*, 118695. [[CrossRef](#)]
24. Dincer, I.; Yüzüak, E.; Elerman, Y. Influence of irreversibility on inverse magnetocaloric and magnetoresistance properties of the $(Ni, Cu)_{50}Mn_{36}Sn_{14}$ alloys. *J. Alloys Compd.* **2010**, *506*, 508–512. [[CrossRef](#)]
25. Gaifullin, R.Y.; Kirilyuk, K.K.; Safarov, I.M.; Musabirov, I.I. Structure of $Ni_{44.4}Mn_{36.2}Sn_{14.9}Cu_{4.5}$ alloy applicable for thermomechanical treatment. *Lett. Mater.* **2023**, *13*, 164–170. [[CrossRef](#)]
26. Nizhankovskii, V.I.; Lugansky, L.B. Vibrating sample magnetometer with a step motor. *Meas. Sci. Technol.* **2007**, *18*, 1533. [[CrossRef](#)]
27. Kresse, G.; Furthmüller, J. Efficient iterative schemes for ab initio total-energy calculations using a plane-wave basis set. *Phys. Rev. B* **1996**, *54*, 11169–11186. [[CrossRef](#)]
28. Kresse, G.; Joubert, D. From ultrasoft pseudopotentials to the projector augmented-wave method. *Phys. Rev. B* **1999**, *59*, 1758–1775. [[CrossRef](#)]

29. Perdew, J.P.; Burke, K.; Ernzerhof, M. Generalized Gradient Approximation Made Simple. *Phys. Rev. Lett.* **1996**, *77*, 3865–3868. [[CrossRef](#)]
30. Ebert, H.; Ködderitzsch, D.; Minár, J. Calculating condensed matter properties using the KKR-Green's function method-recent developments and applications. *Rep. Prog. Phys.* **2011**, *74*, 096501. [[CrossRef](#)]
31. Landau, D.; Binder, K. *A Guide to Monte Carlo Simulations in Statistical Physics*; Cambridge University Press: Cambridge, UK, 2021; p. 578.
32. Koshkid'ko, Y.S.; Dilmieva, E.T.; Cwik, J.; Rogacki, K.; Kowalska, D.; Kamantsev, A.P.; Koledov, V.V.; Mashirov, A.V.; Shavrov, V.G.; Valkov, V.I.; et al. Giant reversible adiabatic temperature change and isothermal heat transfer of MnAs single crystals studied by direct method in high magnetic fields. *J. Alloys Comp.* **2019**, *798*, 810–819. [[CrossRef](#)]
33. Koshkid'ko, Y.S.; Cwik, J.; Ivanova, T.I.; Nikitin, S.A.; Miller, M.; Rogacki, K. Magnetocaloric properties of Gd in fields up to 14 T. *J. Magn. Magn. Mater.* **2017**, *433*, 234–238. [[CrossRef](#)]
34. Moruzzi, V.L.; Janak, J.F.; Schwarz, K. Calculated thermal properties of metals. *Phys. Rev. B* **1988**, *37*, 790–799. [[CrossRef](#)]
35. Sokolovskiy, V.V.; Buchelnikov, V.D.; Zagrebin, M.A.; Entel, P.; Sahool, S.; Ogura, M. First-principles investigation of chemical and structural disorder in magnetic $\text{Ni}_2\text{Mn}_{1+x}\text{Sn}_{1-x}$ Heusler alloys. *Phys. Rev. B* **2012**, *86*, 134418. [[CrossRef](#)]
36. Kuz'min, M.D. Landau-type parametrization of the equation of state of a ferromagnet. *Phys. Rev. B* **2008**, *77*, 184431. [[CrossRef](#)]
37. Gottschall, T.; Skokov, K.P.; Frincu, B.; Gutfleisch, O. Large reversible magnetocaloric effect in Ni-Mn-In-Co. *Appl. Phys. Lett.* **2015**, *106*, 021901. [[CrossRef](#)]
38. Timofeeva, E.; Panchenko, E.; Zherdeva, M.; Tokhmetova, A.; Chumlyakov, Y.I. The Cyclic Stability of the Superelasticity in Quenched and Aged $\text{Ni}_{44}\text{Fe}_{19}\text{Ga}_{27}\text{Co}_{10}$ Single Crystals. *Metals* **2023**, *13*, 1538. [[CrossRef](#)]
39. Bhale, P.; Ari-Gur, P.; Noebe, R.D.; Ren, Y.; Madiligama, A.; Devaraj, R.; Cook, M.S. Effect of Melt-Spinning Parameters on the Structure and Properties of $\text{Ni}_{55.5}\text{Mn}_{18.8}\text{Ga}_{24}\text{Si}_{1.7}$ Heusler Alloy Ribbons. *Materials* **2023**, *16*, 6590. [[CrossRef](#)] [[PubMed](#)]
40. Bachagha, T.; Chakaravarthy, R.; Ren, W.; Saurina, J.; Suñol, J.-J. Structural, Magnetocaloric, and Magnetic Properties in Heusler $\text{Ni}_{50}\text{Mn}_{35}\text{In}_{10}\text{X}_5$ (X = Ga, Fe and Al) Alloys. *Metals* **2023**, *13*, 1913. [[CrossRef](#)]
41. Zhang, Y.; Hao, W.; Hu, C.; Wang, X.; Zhang, X.; Li, L. Rare-Earth-Free $\text{Mn}_{30}\text{Fe}_{20-x}\text{Cu}_x\text{Al}_{50}$ Magnetocaloric Materials with Stable Cubic CsCl-Type Structure for Room-Temperature Refrigeration. *Adv. Funct. Mater.* **2023**, 2310047. [[CrossRef](#)]
42. Zhang, Y.; Xu, P.; Zhu, J.; Yan, S.; Zhang, J.; Li, L. The emergence of considerable room temperature magnetocaloric performances in the transition metal high-entropy alloys. *Mater. Today Phys.* **2023**, *32*, 101031. [[CrossRef](#)]
43. Nambiar, S.S.; Murthy, B.R.N.; Karthik, B.M.; Sharma, S.; Prasanna, A.A. Investigation on Magnetization, Magnetocaloricity, Magnetoresistance, and Electric Properties of Ni-Mn Based Heusler Alloy. *J. Compos. Sci.* **2023**, *7*, 5. [[CrossRef](#)]

Disclaimer/Publisher's Note: The statements, opinions and data contained in all publications are solely those of the individual author(s) and contributor(s) and not of MDPI and/or the editor(s). MDPI and/or the editor(s) disclaim responsibility for any injury to people or property resulting from any ideas, methods, instructions or products referred to in the content.